

Crystal structure of etrasimod,  $C_{26}H_{26}F_3NO_3$ James A. Kaduk<sup>1,2</sup> , Anja Dosen<sup>3</sup>  and Thomas N. Blanton<sup>3</sup> <sup>1</sup>Department of Chemistry, Illinois Institute of Technology, Chicago IL 60616, USA<sup>2</sup>Department of Physics, North Central College, Naperville IL 60540, USA<sup>3</sup>ICDD, Newtown Square, PA, 19073-3273, USA

(Received 24 October 2024; revised 13 January 2025; accepted 14 January 2025)

**Abstract:** The crystal structure of etrasimod has been solved and refined using synchrotron X-ray powder diffraction data and optimized using density functional theory techniques. Etrasimod crystallizes in space group *PI* (#1) with  $a = 10.6131(5)$ ,  $b = 10.7003(5)$ ,  $c = 11.1219(8)$  Å,  $\alpha = 72.756(2)$ ,  $\beta = 76.947(2)$ ,  $\gamma = 77.340(1)^\circ$ ,  $V = 1159.28(6)$  Å<sup>3</sup>, and  $Z = 2$  at 298 K. The crystal structure contains O—H...O hydrogen-bonded etrasimod dimers, which lie in layers approximately parallel to the (2,0,−1) plane. The amino group of each molecule forms an intramolecular N—H...O hydrogen bond to the carbonyl group of the adjacent carboxylic acid group. The powder pattern has been submitted to ICDD for inclusion in the Powder Diffraction File™ (PDF®).

© The Author(s), 2025. Published by Cambridge University Press on behalf of International Center for Diffraction Data. This is an Open Access article, distributed under the terms of the Creative Commons Attribution licence (<http://creativecommons.org/licenses/by/4.0>), which permits unrestricted re-use, distribution and reproduction, provided the original article is properly cited. [doi:10.1017/S0885715625000107]

**Key words:** crystal structure, density functional theory, etrasimod, rietveld refinement, Velsipity®

## I. INTRODUCTION

Etrasimod,  $C_{26}H_{26}F_3NO_3$  (marketed under the trade name Velsipity), is used to treat ulcerative colitis. Etrasimod prevents T cells from entering the bloodstream, thus preventing the T cells from inducing inflammation in body tissues. The systematic name (CAS Registry Number 1206123-37-6) is 2-[(3*R*)-7-[[4-cyclopentyl-3-(trifluoromethyl)phenyl]methoxy]-1,2,3,4-tetrahydrocyclopenta[b]indol-3-yl]acetic acid. A two-dimensional molecular diagram of etrasimod is shown in Figure 1.

Etrasimod is claimed (as Compound 12) in US Patent 8,580,841 B2 (Jones et al., 2013; Arena Pharmaceuticals). A powder pattern for the “2<sup>nd</sup> enantiomer” is reported in the patent, as well as a picture of the molecule from the determination of the crystal structure of the “1<sup>st</sup> enantiomer,” but no atom coordinates are provided. Powder diffraction cannot distinguish between enantiomers, as the necessary information (differences between the intensities of  $hkl$  and  $-h-k-l$  reflections) is completely lost by the overlap of peaks. Powder patterns of the crystalline L-arginine salt of etrasimod are reported in US Patent 10301262B2 (Blackburn et al., 2019; Arena Pharmaceuticals).

This work was carried out as part of a project (Kaduk et al., 2014) to determine the crystal structures of large-volume commercial pharmaceuticals, and include high-quality powder diffraction data for them in the Powder Diffraction File (Kabekkodu et al., 2024).

## II. EXPERIMENTAL

Etrasimod was a commercial reagent, purchased from TargetMol (Batch #148909), and was used as received. The pink powder was packed into a 0.5 mm diameter Kapton capillary and rotated during the measurement at ~2 Hz. The powder pattern was measured at 298(1) K at the Wiggler Low Energy Beamline (Leontowich et al., 2021) of the Brockhouse X-ray Diffraction and Scattering Sector of the Canadian Light Source using a wavelength of 0.819563(2) Å (15.1 keV) from 1.6–75.0°  $2\theta$  with a step size of 0.0025° and a collection time of 3 min. The high-resolution powder diffraction data were collected using eight Dectris Mythen2 X series 1 K linear strip detectors. NIST SRM 660b LaB<sub>6</sub> was used to calibrate the instrument and refine the monochromatic wavelength used in the experiment.

The pattern was indexed using N-TREOR as incorporated into EXPO2014 (Altomare et al., 2013) on a primitive triclinic unit cell with  $a = 10.62303$ ,  $b = 10.70066$ ,  $c = 11.12968$  Å,  $\alpha = 72.734$ ,  $\beta = 77.044$ ,  $\gamma = 77.418^\circ$ ,  $V = 1161.7$  Å<sup>3</sup>, and  $Z = 2$ . Since etrasimod is a chiral molecule, the space group was assumed to be *PI*, which was confirmed by successful solution and refinement of the structure. A reduced cell search of the Cambridge Structural Database (Groom et al., 2016) yielded one hit, but no structures for etrasimod or its derivatives.

The etrasimod molecule was downloaded from PubChem (Kim et al., 2023) as Conformer3D\_COMPOUND\_CID\_44623998.sdf. It was converted to a \*.mol2 file using Mercury (Macrae et al., 2020). The crystal structure was solved by Monte Carlo simulated annealing techniques as implemented in EXPO2014 (Altomare et al., 2013), including a bump penalty on the non-H atoms, using two molecules as fragments.

Corresponding author: James A. Kaduk; Email: [kaduk@polycrystallography.com](mailto:kaduk@polycrystallography.com)



TABLE I. Hydrogen bonds (CRYSTAL23) in etrasimod.

H-Bond	D—H, Å	H...A, Å	D...A, Å	D—H...A, °	Mulliken overlap, <i>e</i>	<i>E</i> , kcal/mol
O5—H59...O65	1.038	1.554	2.587	172.9	0.081	15.6
O64—H118...O6	1.043	1.495	2.535	174.8	0.080	15.5
N7—H50...O6	1.014	2.340*	2.974	119.5	0.013	2.6
N66—H109...O65	1.015	2.278*	2.953	122.7	0.020	3.3
C33—H57...O64	1.103	2.481	3.570	169.0	0.016	
C24—H52...C90	1.092	2.601	3.688	173.4	0.010	
C79—H107...C23	1.104	2.529	3.582	159.0	0.012	

\* = intramolecular.

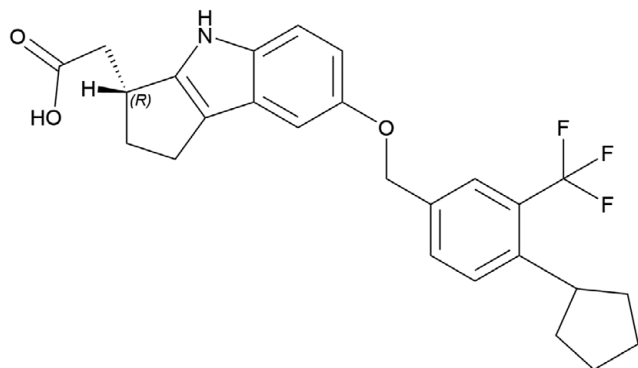


Figure 1. The two-dimensional structure of etrasimod.

Rietveld refinement was carried out with GSAS-II (Toby and Von Dreele, 2013). Only the 4.0–40.0° portion of the pattern was included in the refinements ( $d_{\min} = 1.198$  Å). The coordinates of C22 were fixed to define the origin. All non-H bond distances and angles were subjected to restraints, based on a Mercury/Mogul Geometry Check (Sykes *et al.*, 2011, Bruno *et al.*, 2004). The Mogul average and standard deviation for each quantity were used as the restraint parameters. The phenyl rings and the unsaturated rings of the fused ring

systems were restrained to be planar. The hydrogen atoms were included in calculated positions, which were recalculated during the refinement using Materials Studio (Dassault Systèmes, 2023). The  $U_{\text{iso}}$  of the heavy atoms were grouped by chemical similarity. The  $U_{\text{iso}}$  for the H atoms was fixed at  $1.3 \times$  the  $U_{\text{iso}}$  of the heavy atoms to which they are attached. A few  $U_{\text{iso}}$  refined to slightly negative values, so they were fixed at reasonable values. The peak profiles were described using the generalized (Stephens, 1999) microstrain model. The background was modeled using a 6-term shifted Chebyshev polynomial, with a peak at 10.94° to model the scattering from the Kapton capillary and any amorphous component in the specimen.

The first refinement of 225 variables using 14,401 observations and 188 restraints yielded the residual  $R_{\text{wp}} = 0.05996$ . The Rietveld plot is shown in Figure 2. Even though the fit was reasonable, the model seemed unsatisfactory. The agreement of the Rietveld-refined and DFT-optimized structures was outside the normal range for correct structures ( $< \sim 0.35$  Å); the root-mean-square Cartesian displacements in this first refinement structure were 0.668 and 0.620 Å for molecule 1 and 2 respectively. In molecule 1 there was an intramolecular N—H...O hydrogen bond, but in molecule 2 there was not. The carboxylic acid groups in the two molecules formed a hydrogen bond but

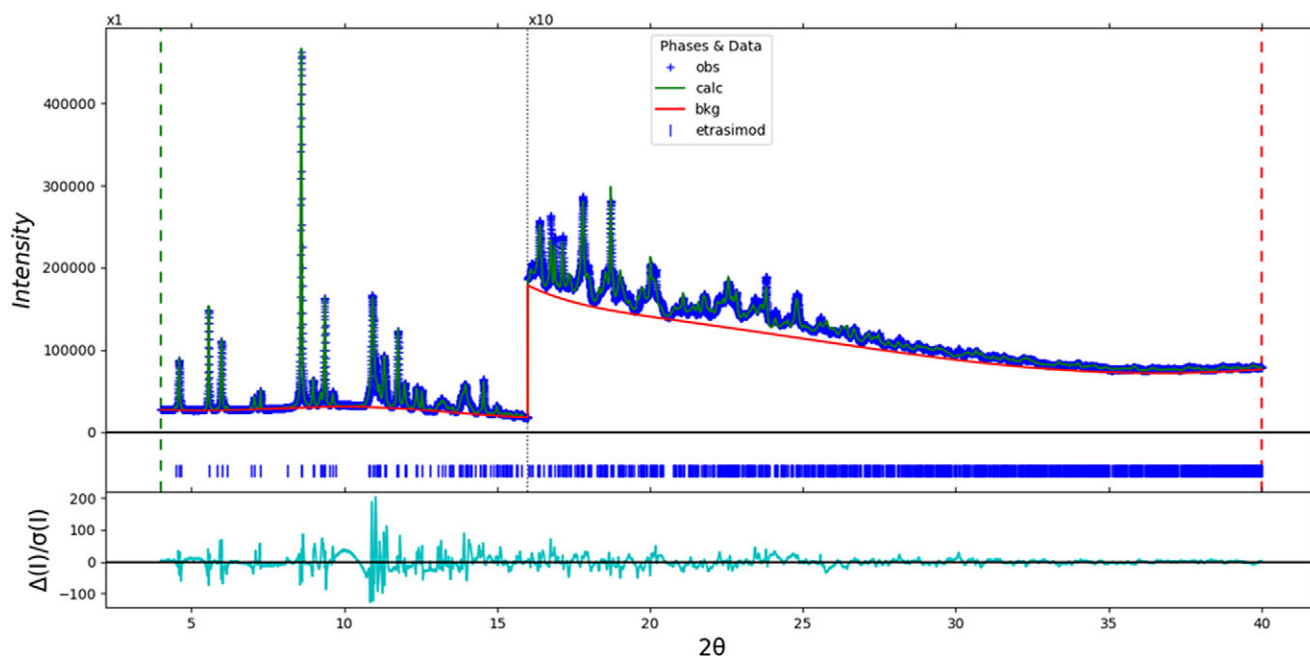


Figure 2. The Rietveld plot for the first incorrect structure of etrasimod ( $R_{\text{wp}} = 0.060$ ). The blue crosses represent the observed data points, and the green line is the calculated pattern. The cyan curve is the normalized error plot, and the red line is the background curve. The vertical scale has been multiplied by a factor of  $10 \times$  for  $2\theta > 16.0^\circ$ .

between the two hydroxyl groups and not a hydroxyl and a carbonyl group. These features seemed chemically unreasonable. We realized that both problems could be solved by rotating the carboxylic acid group in molecule 2 by approximately 180°. This was done in Materials Studio, and a DFT optimization was done. This new model was 18.2 kcal/mol/cell lower in energy than the original model, therefore a new Rietveld refinement was begun from the VASP-optimized structure, using the same strategy as before.

The final refinement of 242 variables using 14,401 observations and 188 restraints yielded the residual  $R_{wp} = 0.03451$ . The restraints contributed 13.0% to the overall  $\chi^2$ . The largest peak (1.01 Å from C33) and hole (1.22 Å from C22) in the difference Fourier map were 0.13(3) and  $-0.13(3)$  eÅ<sup>-3</sup>, respectively. The final Rietveld plot is shown in Figure 3. The largest features in the error plot are in the shapes of some of the strong peaks. These mis-fits probably indicate a change in the specimen during the measurement.

The crystal structure of etrasimod was optimized (fixed experimental unit cell) with density functional theory techniques using VASP (Kresse and Furthmüller, 1996) through the MedeA graphical interface (Materials Design, 2024). The calculation was carried out on 32 cores of a 144-core (768 Gb memory) HPE Superdome Flex 280 Linux server at North Central College. The calculation used the GGA-PBE functional, a plane wave cutoff energy of 400.0 eV, and a  $k$ -point spacing of 0.5 Å<sup>-1</sup> leading to a  $2 \times 2 \times 2$  mesh, and took ~8.2 h. Single-point density functional calculations (fixed experimental cell) and population analysis were carried out using CRYSTAL23 (Erba et al., 2023). (fixed experimental cell) and population analysis were carried out using CRYSTAL17 (Dovesi et al., 2018). The basis sets for the H, C, N, and O atoms in the calculation were those of Gatti et al. (1994), and that for F was that of Peintinger et al. (2013). The calculations were run on a 3.5 GHz PC using 8  $k$ -points and the B3LYP functional and took ~6.5 h.

### III. RESULTS AND DISCUSSION

The agreement of this synchrotron powder diffraction pattern with that reported Jones et al. (2013; Figure 4) is good enough to conclude that they represent the same material.

The root-mean-square Cartesian displacement of the non-H atoms in the Rietveld-refined and VASP-optimized molecules are 0.239 and 0.307 Å for molecules 1 and 2 (Figures 5 and 6); the largest differences are 0.610 Å at C17 and 0.685 Å at O65. The agreement is within the normal range for correct structures (van de Streek and Neumann, 2014). The asymmetric unit is illustrated in Figure 7. The remaining discussion will emphasize the VASP-optimized structure.

Almost all of the bond distances and bond angles fall within the normal ranges indicated by a Mercury Mogul Geometry check (Macrae et al., 2020). Only the C22–C18–C8 (129.0°; average = 122.8(10)°; Z-score = 6.0), C24–C18–C8 (115.0°; average = 120.0(16)°; Z-score = 3.2), and C24–C18–C22 (116.0°; average = 120.2(13)°; Z-score = 3.2) angles are flagged as unusual. The standard uncertainties on the averages are fairly small, inflating the Z-scores. Torsion angles involving rotation about the C8–C18 and C20–C27 bonds are flagged as unusual. The C8–C18 torsions lie on the tails of distributions and reflect the relative orientation of the phenyl and cyclopentyl rings in molecule 1. The C20–C27 torsion lies in valleys of multimodal distributions and reflects the orientation of the carboxylic acid in molecule 1. Molecule 1 seems to be slightly unusual.

Two conformations of the *R* enantiomer of the etrasimod molecule are present (Figure 8). The Mercury Calculate Molecule Overlay tool indicates that the overlap can be improved (rms delta = 0.549 Å) by inverting one of the molecules. PLATON (Spek, 2009, 2020) suggested the presence of a center of symmetry, but refinement of a centrosymmetric model yielded higher residuals ( $R_{wp} \sim 0.058$ ) and some larger  $U_{iso}$ , so the apparent extra symmetry is only approximate.

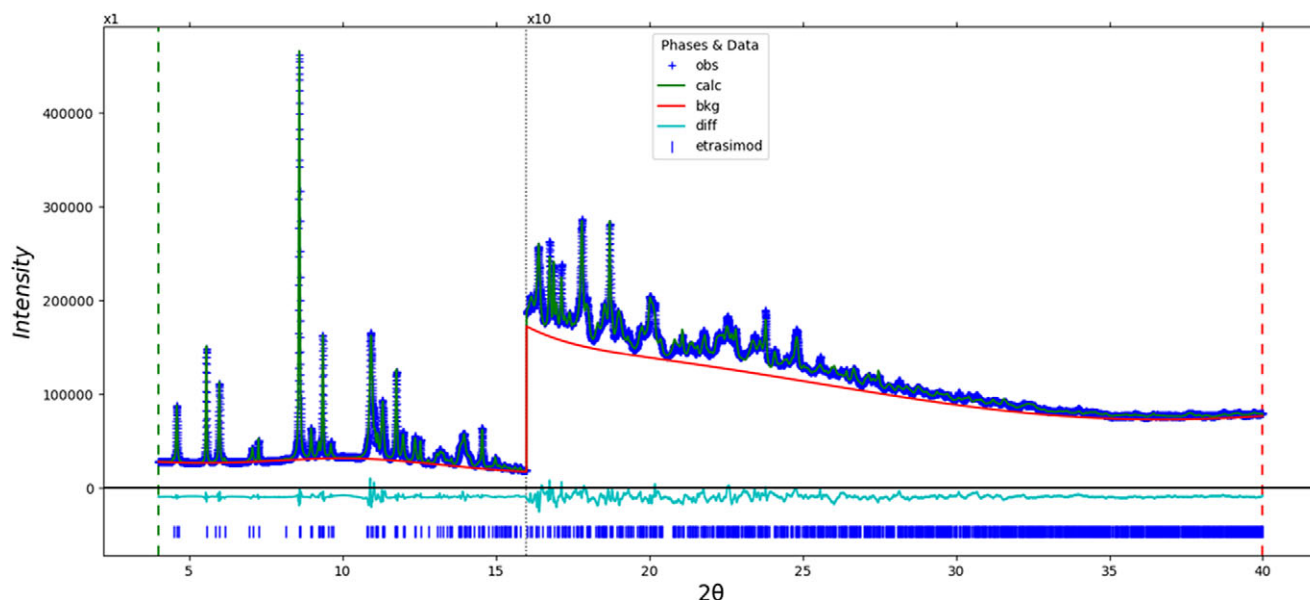


Figure 3. The Rietveld plot for the final structure of etrasimod ( $R_{wp} = 0.034$ ). The blue crosses represent the observed data points, and the green line is the calculated pattern. The cyan curve is the error plot, and the red line is the background curve. The vertical scale has been multiplied by a factor of 10x for  $2\theta > 16.0^\circ$ .

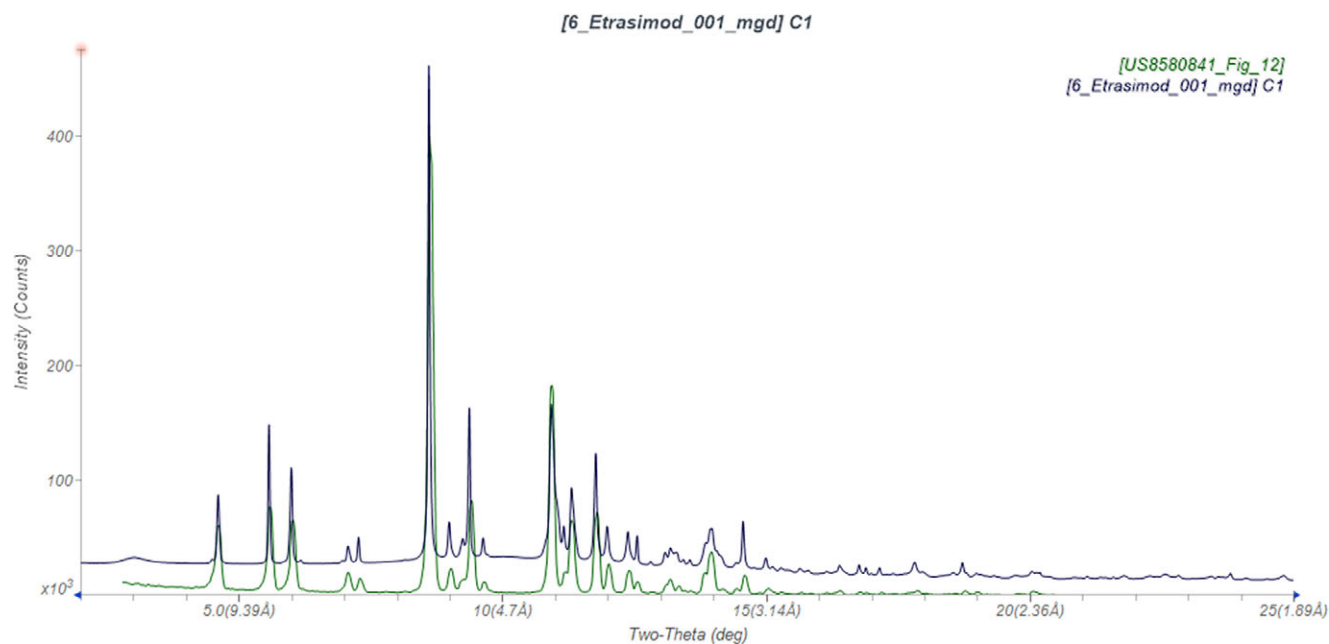


Figure 4. Comparison of the synchrotron pattern of etrasimod (black) collected at the Canadian Light Source to that reported by Jones et al. (2013; green). The literature pattern (Jones et al., 2013; measured using Cu K $\alpha$  radiation) was digitized using UN-SCAN-IT (Silk Scientific, 2013) and converted to the synchrotron wavelength of 0.819563(2) Å using JADE Pro (MDI, 2024). Image generated using JADE Pro (MDI, 2024).

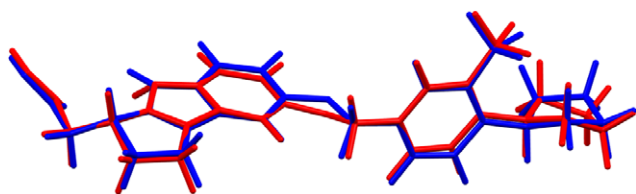


Figure 5. Comparison of the Rietveld-refined (red) and VASP-optimized (blue) structures of molecule 1 of etrasimod. The root-mean-square Cartesian displacement is 0.239 Å. Image generated using Mercury (Macrae et al., 2020).

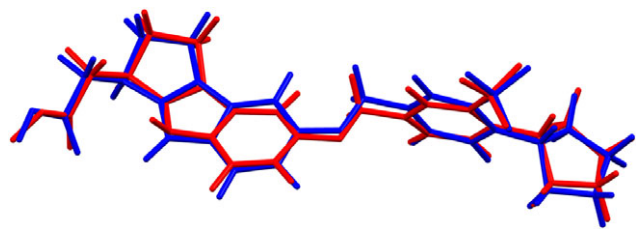


Figure 6. Comparison of the Rietveld-refined (red) and VASP-optimized (blue) structures of molecule 2 of etrasimod. The root-mean-square Cartesian displacement is 0.307 Å. Image generated using Mercury (Macrae et al., 2020).

Quantum chemical geometry optimization of the isolated etrasimod molecules (DFT/B3LYP/6-31G\*/water) using Spartan '24 (Wavefunction, 2023) indicated that molecule 2 is 3.2 kcal/mol lower in energy than molecule 1. Molecule 1 is close to a local minimum-energy conformation; the main difference is in the orientation of the carboxylic acid group. Molecule 2 is close to the global minimum-energy conformation. Intermolecular interactions have a small effect on the observed solid-state conformations.

The crystal structure (Figure 9) contains hydrogen-bonded etrasimod dimers. These dimers extend approximately along the

[689] vector and lie in layers approximately parallel to the (2, 0, −1) plane. The mean planes of the phenyl ring in molecules 1 and 2 are approximately (3, −4, 7) and (4, −4, 7) respectively. The mean planes of the fused ring systems are approximately (18, −1, −11) and (10, 1, −4). The Mercury Aromatics Analyser indicates only weak interactions, with a minimum ring-ring distance of 6.19 Å.

Analysis of the contributions to the total crystal energy of the structure using the Forcite module of Materials Studio (Dassault Systèmes, 2023) indicates that angle distortion terms dominate the intramolecular energy, as might be expected for a fused ring system. The intermolecular energy is dominated by electrostatic attractions, which in this force field-based analysis also include hydrogen bonds. The hydrogen bonds are better discussed using the results of the DFT calculation.

The carboxylic acid group of each molecule forms a strong O—H...O hydrogen bond with the other molecule (Table 1). The result is a dimer, with a graph set (Etter, 1990; Bernstein et al., 1995; Motherwell et al., 2000) R2,2 (8). The energies of the O—H...O hydrogen bonds were calculated using the correlation of Rammohan and Kaduk (2018). The amino group of each molecule forms an intramolecular N—H...O hydrogen bond to the carbonyl group of the adjacent carboxylic acid group. The energies of the N—H...O hydrogen bonds were calculated using the correlation of Wheatley and Kaduk (2019). A surprisingly small number of intermolecular C—H...O and C—H...C hydrogen bonds contribute to the lattice energy.

The volume enclosed by the Hirshfeld surface of etrasimod (Figure 10, Hirshfeld, 1977, Spackman et al., 2021) is 1146.72 Å<sup>3</sup>, 98.92% of half the unit cell volume. The packing density is thus fairly typical. The only significant close contacts (red in Figure 10) involve the hydrogen bonds. The volume/non-hydrogen atom is smaller than normal, at 16.6 Å<sup>3</sup>.



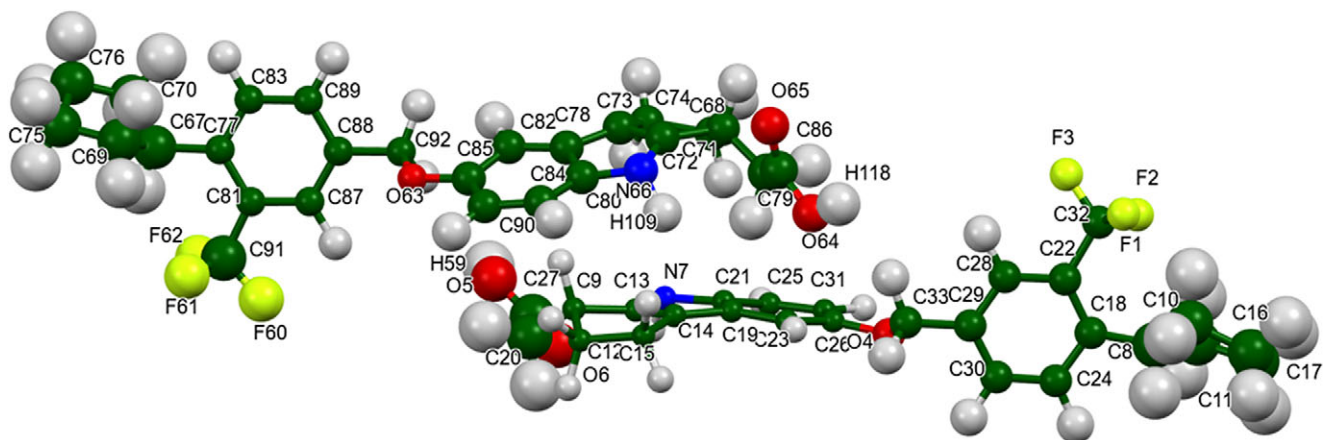


Figure 7. The asymmetric unit of etrasimod, with the atom numbering. The atoms are represented by 50% probability spheroids. Image generated using Mercury (Macrae et al., 2020).

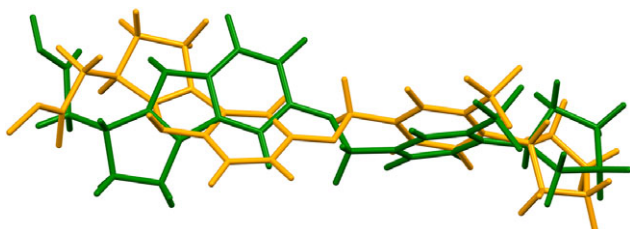


Figure 8. Comparison of molecule 1 (green) and molecule 2 (orange) of etrasimod. Image generated using Mercury (Macrae et al., 2020).

The Bravais–Friedel–Donnay–Harker (Bravais, 1866, Friedel, 1907, Donnay and Harker, 1937) algorithm suggests that we might expect isotropic morphology for etrasimod. A 2<sup>nd</sup>-order spherical harmonic model was included in the refinement. The texture index was 1.010(0), indicating that the preferred orientation was not significant in this rotated capillary specimen.

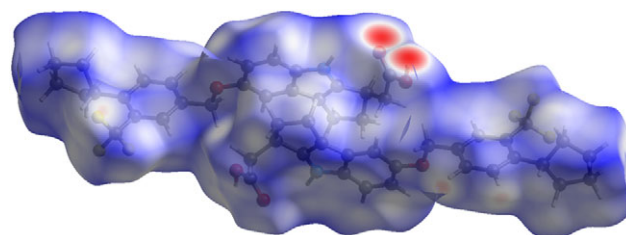


Figure 10. The Hirshfeld surface of etrasimod. Intermolecular contacts longer than the sums of the van der Waals radii are colored blue, and contacts shorter than the sum of the radii are colored red. Contacts equal to the sums of radii are white. Image generated using CrystalExplorer (Spackman et al., 2021).

## DEPOSITED DATA

The powder pattern of etrasimod from this synchrotron data set has been submitted to ICDD for inclusion in the Powder Diffraction File. The Crystallographic Information

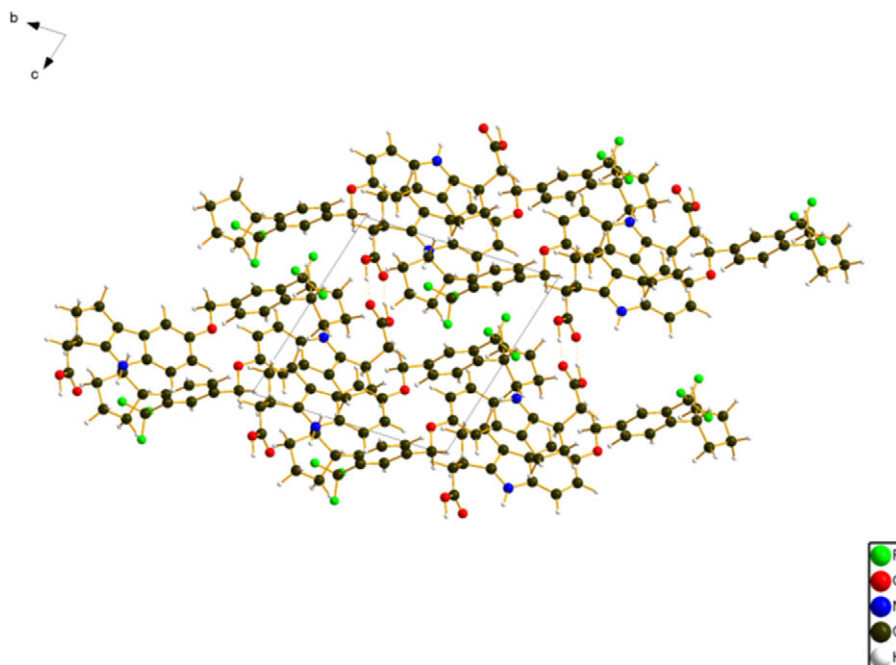


Figure 9. The crystal structure of etrasimod, is viewed down the *a*-axis. Image generated using Diamond (Crystal Impact, 2023).

Framework (CIF) files containing the results of the Rietveld refinement (including the raw data) and the DFT geometry optimization were deposited with the ICDD. The data can be requested at [pdj@icdd.com](mailto:pdj@icdd.com).

## ACKNOWLEDGMENTS

Part or all of the research described in this paper was performed at the Canadian Light Source, a national research facility of the University of Saskatchewan, which is supported by the Canada Foundation for Innovation (CFI), the Natural Sciences and Engineering Research Council (NSERC), the Canadian Institute of Health Research (CIHR), the Government of Saskatchewan, and the University of Saskatchewan. This work was partially supported by the International Centre for Diffraction Data. We thank Adam Leontowich for his assistance in the data collection. We also thank the ICDD team – Megan Rost, Steve Trimble, and Dave Bohnenberger – for their contribution to research, sample preparation, and in-house XRD data collection and verification.

## CONFLICT OF INTEREST

The authors have no conflicts of interest to declare.

## REFERENCES

- Altomare, A., C. Cuocci, C. Giacovazzo, A. Moliterni, R. Rizzi, N. Corriero, and A. Falcicchio. 2013. "EXPO2013: A Kit of Tools for Phasing Crystal Structures from Powder Data." *Journal of Applied Crystallography* 46: 1231–1235.
- Bernstein, J., R. E. Davis, L. Shimoni, and N. L. Chang. 1995. "Patterns in Hydrogen Bonding: Functionality and Graph Set Analysis in Crystals." *Angewandte Chemie International Edition in English* 34: 1555–1573.
- Blackburn, A. C., R. O. Castro, M. A. Hadd, Y.-A. Ma, A. G. Montalban, J. K. Rueter, L. A. Selvey, S. R. Shakyia, and M. Carlos. 2019. "Crystal-line L-Arginine Salt of (R)-2-(7-(4-Cyclopentyl-3-(Trifluoromethyl) Benzyloxy)-1,2,3,4-Tetrahydrocyclopenta[b]indol-3-yl)Acetic Acid (Compound 1) for Use in SIPI Receptor-Associated Disorders." United State Patent 10301262 B2.
- Bravais, A. 1866. *Etudes Cristallographiques*. Paris, Gauthier Villars.
- Bruno, I. J., J. C. Cole, M. Kessler, J. Luo, W. D. S. Motherwell, L. H. Purkis, B. R. Smith, R. Taylor, R. I. Cooper, S. E. Harris, and A. G. Orpen. 2004. "Retrieval of Crystallographically-Derived Molecular Geometry Information." *Journal of Chemical Information and Computer Sciences* 44: 2133–2144.
- Crystal Impact. 2023. *Diamond V. 5.0.0*. Bonn, Germany. Crystal Impact - H. Putz & K. Brandenburg.
- Dassault Systèmes. 2023. *BIOVIA Materials Studio 2024*. San Diego, CA. BIOVIA.
- Donnay, J. D. H., and D. Harker. 1937. "A New Law of Crystal Morphology Extending the Law of Bravais." *American Mineralogist* 22: 446–467.
- Erba, A., J. K. Desmarais, S. Casassa, B. Civalleri, L. Donà, I. J. Bush, B. Searle, L. Maschio, L.-E. Daga, A. Cossard, C. Ribaldone, E. Ascrizzi, N. L. Marana, J.-P. Flament, and B. Kirtman. 2023. "CRYSTAL23: A Program for Computational Solid State Physics and Chemistry." *Journal of Chemical Theory and Computation* 19: 6891–6932; <https://doi.org/10.1021/acs.jctc.2c00958>.
- Etter, M. C. 1990. "Encoding and decoding hydrogen-bond patterns of organic compounds." *Accounts of Chemical Research* 23: 120–126.
- Friedel, G. 1907. "Etudes sur la loi de Bravais." *Bulletin de la Société Française de Minéralogie* 30: 326–455.
- Gatti, C., V. R. Saunders, and C. Roetti. 1994. "Crystal-Field Effects on the Topological Properties of the Electron-Density in Molecular Crystals – the Case of Urea." *Journal of Chemical Physics* 101: 10686–10696.
- Groom, C. R., I. J. Bruno, M. P. Lightfoot, and S. C. Ward. 2016. "The Cambridge Structural Database." *Acta Crystallographica Section B: Structural Science, Crystal Engineering and Materials* 72: 171–179.
- Hirshfeld, F. L. 1977. "Bonded-Atom Fragments for Describing Molecular Charge Densities." *Theoretica Chimica Acta* 44: 129–138.
- Jones, R. M., D. J. Buzzard, S. Han, S. H. Kim, J. Lehmann, B. Ullman, J. V. Moody, X. Zhu, and S. Stirn. 2013. "Substituted 1,2,3,4-Tetrahydrocyclopenta[b]indol-3-yl)Acetic Acid Derivatives Useful in the Treatment of Autoimmune and Inflammatory Disorders." United States Patent 8580841B2.
- Kabekkodu, S., A. Dosen, and T. N. Blanton. 2024. "PDF-5+: A Comprehensive Powder Diffraction File™ for Materials Characterization." *Powder Diffraction* 39: 47–59.
- Kaduk, J. A., C. E. Crowder, K. Zhong, T. G. Fawcett, and M. R. Suchomel. 2014. "Crystal Structure of Atomoxetine Hydrochloride (Strattera), C<sub>17</sub>H<sub>22</sub>NOCl." *Powder Diffraction* 29: 269–273.
- Kim S., J. Chen, T. Cheng, A. Gindulyte, J. He, S. He, Q. Li, B. A. Shoemaker, P. A. Thiessen, B. Yu, L. Zaslavsky, J. Zhang, and E. E. Bolton. 2023. "PubChem 2023 update." *Nucleic Acids Research* 51: D1373–D1380; doi:10.1093/nar/gkac956.
- Kresse, G., and J. Furthmüller. 1996. "Efficiency of Ab-Initio Total Energy Calculations for Metals and Semiconductors Using a Plane-Wave Basis Set." *Computational Materials Science* 6: 15–50.
- Leontowich, A. F. G., A. Gomez, B. Diaz Moreno, D. Muir, D. Spasyuk, G. King, J. W. Reid, C.-Y. Kim, and S. Kycia. 2021. "The Lower Energy Diffraction and Scattering Side-Bounce Beamline for Materials Science at the Canadian Light Source." *Journal of Synchrotron Radiation* 28: 1–9; <https://doi.org/10.1107/S1600577521002496>.
- Macrae, C. F., I. Sovago, S. J. Cottrell, P. T. A. Galek, P. McCabe, E. Pidcock, M. Platings, G. P. Shields, J. S. Stevens, M. Towler, and P. A. Wood. 2020. "Mercury 4.0: From Visualization to Design and Prediction." *Journal of Applied Crystallography* 53: 226–235.
- Materials Design. 2024. *Medea 3.7.2*. San Diego, CA, Materials Design Inc.
- MDI. 2024. *JADE Pro version 9.0*. Livermore, CA, Materials Data.
- Motherwell, W. D. S., G. P. Shields, and F. H. Allen. 2000. "Graph-Set and Packing Analysis of Hydrogen-Bonded Networks in Polyamide Structures in the Cambridge Structural Database." *Acta Crystallographica B* 56: 857–871.
- Peintinger, M. F., D. Vilela Oliveira, and T. Bredow, T. 2013. "Consistent Gaussian Basis Sets of Triple-Zeta Valence with Polarization quality for Solid-State Calculations." *Journal of Computational Chemistry* 34: 451–459.
- Rammohan, A. and J. A. Kaduk. 2018. "Crystal Structures of Alkali Metal (Group 1) Citrate Salts." *Acta Crystallographica Section B: Crystal Engineering and Materials* 74: 239–252.
- Silk Scientific. 2013. *UN-SCAN-IT 7.0*. Orem, UT, Silk Scientific Corporation.
- Spackman, P. R., M. J. Turner, J. J. McKinnon, S. K. Wolff, D. J. Grimwood, D. Jayatilaka, and M. A. Spackman. 2021. "CrystalExplorer: A Program for Hirshfeld Surface Analysis, Visualization and Quantitative Analysis of Molecular Crystals." *Journal of Applied Crystallography* 54: 1006–1011; <https://doi.org/10.1107/S1600576721002910>; <https://crystalexplorer.net>.
- Spek, A. L. 2009. "Structure Validation in Chemical Crystallography." *Acta Crystallographica D* 65: 148–155.
- Spek, A. L. 2020. "CheckCIF Validation Alerts: What They Mean and How To Respond." *Acta Crystallographica E* 76: 1–11.
- Stephens, P. W. 1999. "Phenomenological Model of Anisotropic Peak Broadening in Powder Diffraction." *Journal of Applied Crystallography* 32: 281–289.
- Sykes, R. A., P. McCabe, F. H. Allen, G. M. Battle, I. J. Bruno, and P. A. Wood. 2011. "New Software for Statistical Analysis of Cambridge Structural Database Data." *Journal of Applied Crystallography* 44: 882–886.
- Toby, B. H., and R. B. Von Dreele. 2013. "GSAS II: The Genesis of a Modern Open Source All Purpose Crystallography Software Package." *Journal of Applied Crystallography* 46: 544–549.
- van de Streek, J., and M. A. Neumann. 2014. "Validation of Molecular Crystal Structures from Powder Diffraction Data with Dispersion-Corrected Density Functional Theory (DFT-D)." *Acta Crystallographica Section B: Structural Science, Crystal Engineering and Materials* 70: 1020–1032.
- Wavefunction, Inc. 2023. *Spartan '24. V. 1.0.0*. Irvine CA. Wavefunction Inc.
- Wheatley, A. M., and J. A. Kaduk. 2019. "Crystal Structures of Ammonium Citrates." *Powder Diffraction* 34: 35–43.